SPRINGER LINK

Log in

☰ Menu   🔍 Search

🛒 Cart

Doping Effect of Fe Ions on the Structural, Electrical, and Magnetic Properties of SrTiO₃ Nanoceramic Matrix

Download PDF ⤓

Journal of Superconductivity and Novel Magnetism

Aims and scope

Submit manuscript

Dhananjay N. Bhoyar, Jitendra S. Kounsalye, Pankaj P. Khirade, A. A. Pandit & K. M. Jadhav ✉

Abstract

In the present investigation, strontium titanate nanoceramic was synthesized by incorporating iron (Fe) ion with general formula $SrTi_{1-x}Fe_xO_3$ (x = 0.0, 0.1, 0.2, and 0.4) using sol-gel autocombustion method. The effect of Fe ions on the structural, morphological, electrical, dielectric, and magnetic properties of the prepared matrix has been investigated by

various characterization techniques with the appropriate formulation. The structural properties such as phase space, crystallite size (D), and lattice parameter (a) of prepared matrix are calculated by X-ray diffraction (XRD) technique. The functional groups were analyzed by Fourier transform infrared spectroscopy (FT-IR). The surface morphology of the prepared nanoceramic matrix has been determined by using field emission scanning electron microscopy (FE-SEM) analysis. Calculation of average particle size and diffraction patterns was confirmed by using images from transmission electron microscopy (TEM) and selected area electron diffraction pattern (SAED), respectively. An energy dispersive spectrum analysis (EDS) confirmed the compositional stoichiometry in the investigated matrix. Electrical conductivity increased the prepared sample due to the increasing in the Fe concentration and temperature. The dielectric parameters in the frequency range of 30 Hz to 1 MHz were found higher at lower frequencies. The pure $SrTiO_3$ matrix shows a paramagnetic nature at room temperature, but for a higher concentration of Fe doping was used to observe the weak ferromagnetic nature. Therefore, due to Fe ion concentration, the properties of the prepared matrix have been completely varied and enhancement in the magnetic properties was observed.
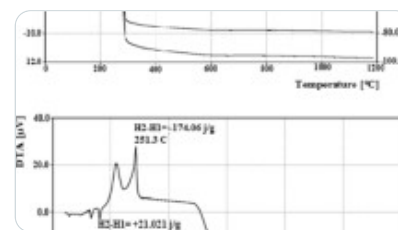
Similar content being viewed by others
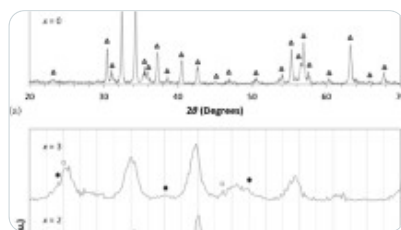
Structure and magnetic properties of Zr−Mn substituted strontium hexaferrite Sr(Zr,Mn) x...

Article | 23 August 2016
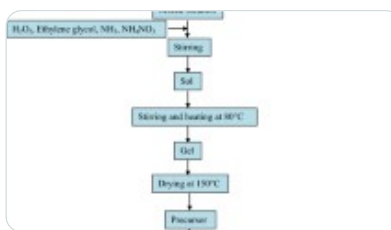
Effect of precursors on the structural, magnetic, dielectric, microwave and electromagnetic...

Article | 19 September 2019

A Study of the Morlogical Properties of SrFe12−xCoxO19 (x = 0, 0.1, 0.2) Hexaferrite...

Article | 05 December 2014

Use our pre-submission checklist →

Avoid common mistakes on your manuscript.

1 Introduction

Perovskite-structured ceramic materials have versatile and extraordinary features like ferroelectric, pyroelectric, piezoelectric, dielectric, ferromagnetic, magnetocaloric, and superconducting properties which can be applied in advanced science and technology [1,2,3]. Therefore, their demand for various applications in industries and modern electronic devices is increased. The multifunctional perovskite material provides the required electrical and magnetic properties for modern electronic devices in the single system. Among the perovskite family, strontium titanate ($SrTiO_3$) and barium titanate ($BaTiO_3$) are most significant and promising materials commonly used in the nonlinear optical field as a pyroelectric detector [4, 5], electrooptics modulator, thin film capacitors, and optical memory devices [6].

Ternary oxide $SrTiO_3$ nanoceramic material, after nucleation and crystal growth, becomes a perovskite cubic structure. $SrTiO_3$ has mixed ionic-covalent bonding that makes a unique structure, which leads to the best electronic material. $SrTiO_3$ perovskite has potential applications in various fields such as random access memory, photocatalysts, ferroelectrics, and reproducible switching in the leakage current [7,8,9], giant photo-induced dielectric constant at low temperatures, reversible laser photoluminescence, and reversible photo-induced spectral changes [10]. These properties of $SrTiO_3$ are dependent on the structure, size, and shape [5, 11]. The nanoscale properties of the perovskite materials are found to be better as compared with bulk form which can be enhanced by the changing synthesis method, sintering temperature, pressure, chelating agent, pH, etc. [11,12,13,14]. In order to get a further modification in characteristic properties of $SrTiO_3$, nanoceramic materials can be obtained with the help of partial substitution of the cations at both sites. The cations should maintain the stability of unusual mixed oxidation states in the crystal structure. Several researchers reported that the substitutions of donor or acceptor impurities in perovskite materials will increase the majority charge of the carriers [15, 16].

By introducing trivalent atoms like Fe in B site of $SrTiO_3$, oxygen vacancies will be formed which may be due to the difference in oxidation states of cations Fe^{3+} and Ti^{4+} of B site. These oxygen vacancies created help in maintaining the charge balance and increase the concentration of majority charge carriers, i.e., holes. Also, it can be beneficial to design high-sensitivity oxygen sensors due to the decrease in the electrical resistivity of the material [17,

18]. $SrTiO_3$ materials are widely used in microelectronic devices due to its advanced dielectric properties and thermodynamic stability at high temperature [19,20,21]. To increase the induced ferromagnetism in materials like $SrTiO_3$, addition of magnetic impurities (Fe, Co, and Mn) can be applicable for spintronic devices [22]. Therefore, new mechanisms have to be proposed to explain the transport and magnetic behavior. Also, Fe-doped $SrTiO_3$ materials can be applicable for photocatalytic activity, nonlinear optical materials, gas sensing material, and a phase shifter in communication systems [21, 23,24,25]. Fe-doped $SrTiO_3$ materials are given much attention due to their wide range of potential applications and versatile behavior. These properties of $SrTiO_3$ inspire us to investigate the structural, morphological, electrical, dielectric, and magnetic property of Fe–doped $SrTiO_3$.

In the present investigation, Fe-doped $SrTiO_3$ nanoceramics have been prepared by adopting the sol-gel autocombustion method. The impact of Fe doping on structural, morphological, electrical, dielectric, and magnetic properties has been studied. The frequency-dependent dielectric properties of the prepared samples in the frequency range from 30 Hz to 1 MHz have been investigated, and the DC electrical conductivity has been analyzed to determine the Fe effect on the conduction mechanisms.

2 Experimental Details

2.1 Materials and Synthesis

Strontium nitrate hexahydrate ($Sr(NO_3)_2 \cdot 6H_2O$), tetra-butyl titanate ($Ti(OC_4H_9)_4$), citric acid ($C_6H_8O_7$), ferric nitrate nonahydrate ($Fe(NO_3)_3 9H_2O$), ethanol (C_2H_5–OH), and ammonium hydroxide (NH_4OH) were procured from Merck with ~ 99% purity and used as starting materials without further purification.

Sol-gel autocombustion techniques has been adapted for the synthesis of $SrTi_{1-x}Fe_xO_3$ (x = 0.0, 0.1, 0.2, and 0.4) nanoceramic material. Initially, tetra-butyl titanate solution in a glass beaker was dissolved with a chelating agent, ethanol, and added into the citric acid aqueous solution. The prepared mixture of the solution was adjusted to pH = 8 by adding the appropriate amount of ammonia. Further, this mixture was stirred at 80 °C for 1 h and produced a yellowish transparent liquid which is marked as solution "A." Subsequently, strontium nitrate

and ferric nitrate were separately dissolved in 100 ml of distilled water with continuous stirring until the homogeneous solution was prepared and marked as solution "B." Both solutions A and B were mixed together by adjusting pH value at 7 using the ammonia solution with continuous stirring for 3 h

The prepared solution gradually becomes viscous and then a stable, transparent solution was formed. The same solution was produced by continuous heating at 110 °C; the gel formation took place and viscous gel transforms into a dry gel. The autocatalytic nature of the combustion process of nitrate−citric acid gel was observed, and the experimental observations showed that the dried gel formed from metal nitrates and citric acid exhibited a self-propagating combustion behavior. The entire combustion process was carried out in the very short interval of time. The obtained ash was dried and crushed for 1 h to get well-resolved powder sample. The annealing of this powder sample was done at 900 °C for 5 h.

2.2 Characterizations

The crystalline phase of the prepared matrix at room temperature was examined by X-ray diffraction (XRD) technique Ultima IV of Rigaku Corporation, Japan. The XRD pattern was recorded using nickel-filtered Cu-Kα radiation (λ = 1.5418 Å) in the 2θ range of 20−80° with a stepsize of 0.01°. The morphology of the samples was studied by Hitachi Model-S-4800 field emission scanning electron microscopy (FE-SEM) operated at 20 kV. The elemental analysis was carried by energy dispersive spectroscopy (EDS) which is attached to FE-SEM. The powders were mixed with a polyvinyl alcohol (PVA) agent as a binder and pressed into cylindrical pellets with a 10-mm diameter and 3-mm thickness under the a 50-MPa pressure. The pellets were sintered in a muffle furnace at 900 °C for 1 h for removal of binder and used for bulk density, electrical, and dielectric measurements. In order to get good ohmic contacts, these pellets were coated with silver paste on the smooth surface of both the parallel ends. Using the standard two-probe method, the DC electrical conductivity of all samples was measured. The dielectric properties of all the samples were measured using the LCR-Q meter (Hioki 3532-50, Japan) as a function of frequencies. Magnetic properties were studied by vibrating sample magnetometer (VSM) (Lakeshore VSM 7410).

3 Results and Discussion

3.1 X-ray Diffraction

The X-ray diffraction pattern of synthesized $SrTi_{1-x}Fe_xO_3$ nanoceramics with composition x = 0.0, 0.1, 0.2, and 0.4 is shown in Fig. 1. From the XRD pattern analysis of $SrTi_{1-x}Fe_xO_3$ nanoceramics, it was found that all the existing peaks (100), (110), (111), (200), (210), (211), and (220) is well matched with the standard pure $SrTiO_3$ (JCPDS No. 89–4934) of *Pm3m* space group [26]. The XRD pattern envisaged that the small amount of impurity phase of TiO_2 is due to the replacement of Ti ions by Fe ions. From the XRD analysis, interplanar distance (d) was determined by appropriate 2θ values of intense peaks using Bragg's law. Lattice constant (a) for each corresponding peak in XRD pattern is calculated by using the following relation [27].

Fig. 1
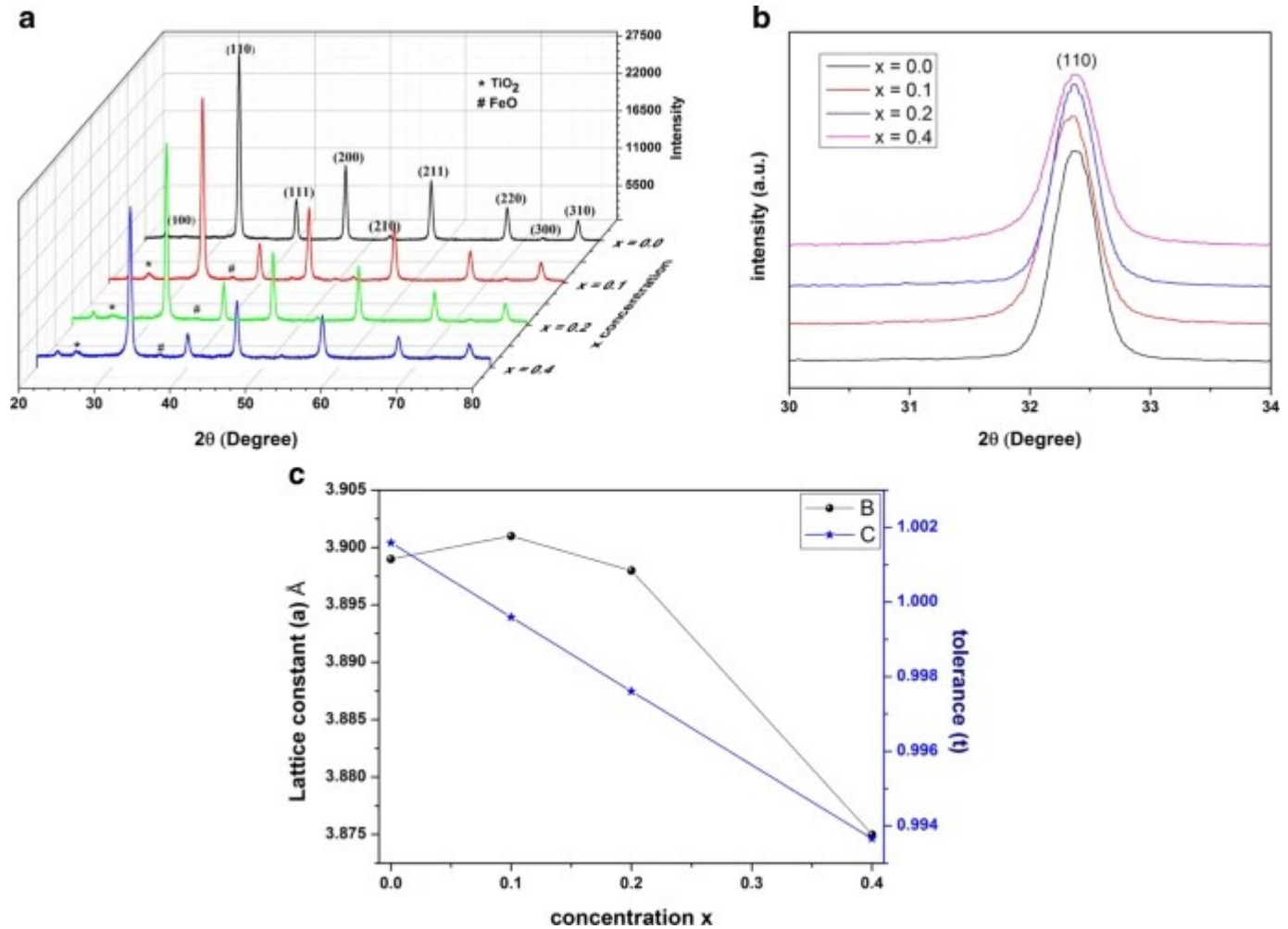
a X-ray diffraction patterns of SrTi$_{1-x}$Fe$_x$O$_3$ (x = 0.0, 0.1, 0.2, and 0.4) nanoceramic. b Shifting 2θ in XRD patterns of SrTi$_{1-x}$Fe$_x$O$_3$ (x = 0.0, 0.1, 0.2, and 0.4) nanoceramic for (110) peak. c Variation of lattice constant and tolerance of SrTi$_{1-x}$Fe$_x$O$_3$ (x = 0.0, 0.1, 0.2, and 0.4) nanoceramic

$$ \frac{1}{d^{2}}=\frac{h^{2}+k^{2}+l^{2}}{a^{2}} $$

(1)

The graph between the lattice parameter (a) of each reflection plane in the sample is plotted more accurately using Nelson–Riley extrapolation function (N–R) and given the formula.

$$ F(\theta)=\frac{1}{2}[(\frac{{\cos}^{2}\theta} {\sin\theta})+(\frac{{\cos}^{2}\theta} $$

{\theta})] $$

(2)

The lattice constant (a) initially increases for x = 0.1 due to the addition of Fe^{3+} cations of high ionic radii of 0.645 Å as compared with Ti^{4+} ions at 0.605 Å on B-site in $SrTiO_3$ matrix. Whereas for higher concentration of x = 0.2 and 0.4, the lattice parameter decreases due to the change in oxidation state of Fe ions with a variation in ionic radii of Fe^{3+} (0.645 Å) and Fe^{4+} (0.585 Å) on the B site of $SrTiO_3$ [28].

Figure 1b reveals the comparison of the relative peak intensity with the 2θ range of 31−33° for the pure and doped samples. The peak intensity of doped samples decreased with increasing Fe concentrations which demonstrate the samples in less crystalline form as compared with the pure sample due to the (110) Bragg's reflection [28]. The influence of Fe^{3+} concentration in $SrTiO_3$ matrix shows the shifting in diffraction angle of Bragg's reflection plane (110), but no double peaks were observed in the 45−48° range, which suggests that there is no phase change in the original cubic perovskite structure.

The average crystallite sizes (D) of all the prepared samples were calculated from Debye Scherrer's formula by using the broadening of XRD peaks and corrected by microstrain Williamson–Hall (W–H) plots. The maximum intensity area (A), centered peak, and FWHM for diffraction angle θ was obtained with the help of Gaussian fitting of respective XRD peaks. The instrumental broadening (β) was corrected by using the formula;

$$ \beta =\beta_{\text{obs}}-\beta_{\text{ins}} $$

(3)

where β_{obs} is the observed FWHM from the XRD pattern and β_{ins} the FWHM of the standard sample. The lattice strain or the microstrain was determined using the W–H plot and which is according to the following expression [29];

$$ \frac{\beta \cos\theta} {\lambda} =\frac{k}{D}+\varepsilon \frac{\sin\theta} {\lambda} $

$

(4)

The graphs between $\frac{\beta \cos \theta}{\lambda}$ versus $\frac{\sin \theta}{\lambda}$ give a straight line with slope (ε) which gives a direct microstrain. The D can be calculated by using slope obtained from the graph [30];

$$ D=\frac{0.89}{\text{intercept}} $$

(5)

The average crystallite size was found in 16 to 28 nm range. The variation of lattice constant (a), average D, and microstrain (ε) with a doping concentration is summarized in Table 1. The intrinsic strain is changed monotonically with the doping concentrations due to the change in the microstructure, size, and shape of the particles. The other structural parameters such as X-ray density (ρ_x), bulk density (ρ_B), and porosity ($P\%$) were calculated using relations (6), (7), and (8), respectively [31], and their values are given in Table 1.

$$ \rho_{x}=\frac{ZM}{N_{A}V} $$

(6)

where Z is the number of formula units in the unit cell ($Z=1$), M is the molecular mass of the sample, and N_A is the Avogadro's number. X-ray density range from 5.140 to 5.327 g cm^{-3}. The ρ_B of the pellets can be measured by using the Archimedes method in that water is used immersion liquid ($\rho = 0.997$ g cm^{-3}); bulk density can be expressed by the following relation:

$$ \rho_{B}=\frac{W_{\text{dry}}}{W_{\text{wet}}-W_{\text{sus}}}\times d_{\mathrm{H}_{2}\mathrm{O}} $$

(7)

where W_{wet} and W_{dry} are wet and dry weights of the pellets subsequently measured in the air

before and after drying at 100 °C for 24 h, and W_{sus} is the suspended weight in water of each pellet. The ρ_B values were lower as compared with ρ_x, and its lower value was attributed to the pore formation during synthesis processes. The values of ρ_x and ρ_B were used to obtain the percentage porosity $P\%$ (closed porosity) of all the samples;

$$ P\% = 1-\frac{\rho_{B}}{\rho_{x}} $$

(8)

where ρ_B are ρ_x are bulk density and X-ray density, respectively. The porosity of the present composition increases with doping concentration which can be related to their microstructure. The total porosity level, pore connectivity, material composition, and microstructural homogeneity have a significant influence on electrical and dielectric properties.

Table 1 Lattice constant (a), bulk density (ρ_B), X-ray density (ρ_x), porosity (P), unit cell volume (V), micro-strain (ε), crystallite size (D), and tolerance factor ($t^{\prime}$) of $SrTi_{1-x}Fe_xO_3$ ($x = 0.0, 0.1, 0.2,$ and 0.4) nanoceramics

---

The formability of the perovskite structure can be well explained trough calculation with the help of tolerance factor ($t^{\prime}$) suggested by Goldschmidt which can be expressed as [32];

$$ t^{\prime}=\frac{(r_{A}+r_{o})}{\sqrt 2 (r_{B}+r_{o})} $$

(9)

where r_A and r_B are the ionic radii of the A and B cations, while r_O is the ionic radii of oxygen anion (Å). For calculating the tolerance factor, Shannon's ionic radii of Sr^{2+} (1.61 Å), Ti^{4+} (0.605 Å), and O^{2-} (1.35 Å) were used. The values of the tolerance factors were found to decrease with increase in the doping concentration, as shown in Table 1, which confirms the present composite matrix in the perovskite structure.

3.2 Fourier Transform Infrared Spectroscopy

Figure 2 shows the FT–IR spectrum of prepared samples. Generally, the transmittance band in ABO_3 perovskite is observed in the wavenumber range of $450-650$ cm^{-1} due to the stretching vibrations of metal–oxygen (O–M–O) in B-site. In the present matrix, this band corresponds to the stretching vibrations of Ti–O bond, and it confirms blue shift due to the doping concentration of Fe ions [33]. The absorption peak near $1426-1492$ cm^{-1} corresponds to the deformation mode of absorbed water (H_2O) molecules. From FT–IR spectra, there is shifting of bands for the Fe-doped $SrTiO_3$ samples for higher Fe concentration due to the change in the ionic radii of Fe ions and change in cell size. The vibrational frequency of Fe/Ti–O bond can be determined by the following relation [34].

$$ \bar{\nu} = \frac{1}{2\pi c}\sqrt{\frac{k}{\mu}} $$

(10)

where, $\bar{\nu}$, k, and c represent the wave number, average molecular force constant, and the velocity of light, and effective mass μ of the Fe/Ti–O bond can be obtained by the following relation [34].
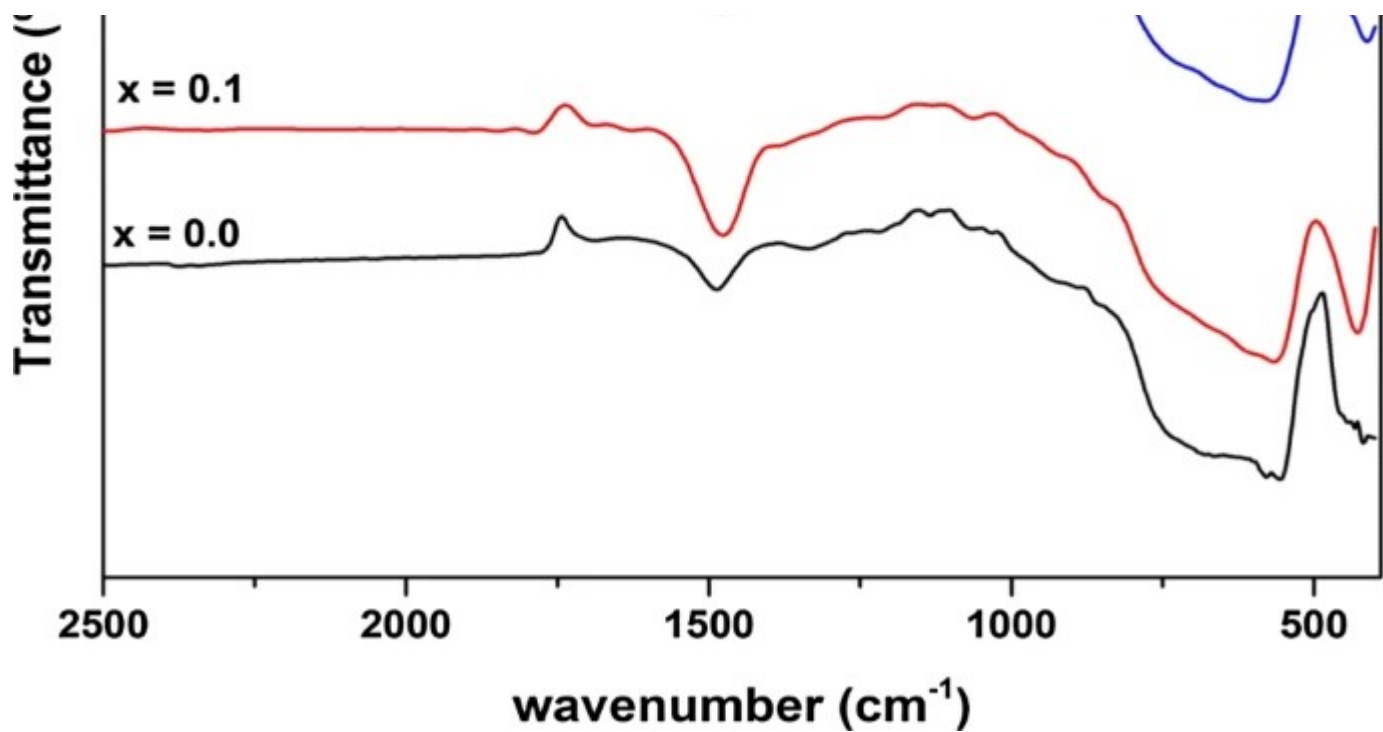
$$ \mu = \frac{M_{0}\times [(1-x)M_{\text{Ti}}+xM_{\text{Fe}}]}{M_{0}+[(1-x)M_{\text{Ti}}+xM_{\text{Fe}}]} $$

(11)

where, M_0, M_{Ti}, and M_{Fe} are the atomic weight of oxygen, titanium, and iron, respectively.

Fig. 2
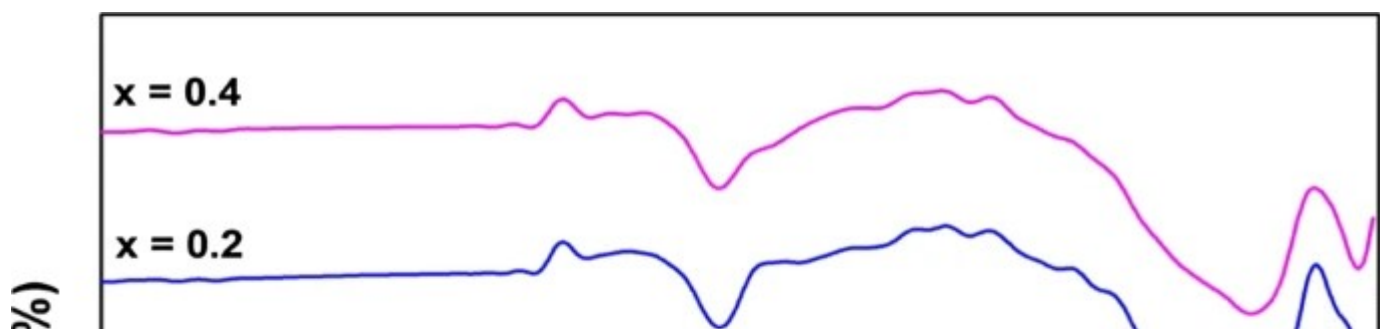
FTIR spectra of $SrTi_{1-x}Fe_xO_3$ (x = 0.0, 0.1, 0.2, and 0.4) nanoceramic

Force constant can be determined from the bond length of Fe/Ti−O.

$$ k=\frac{17}{r^{3}} $$

(12)

The value of force constant and the average bond length of Fe/Ti−O are summarized in Table 2; due to doping of Fe, the bond length decreases and interaction between Ti and O atom increases.

Table 2 Wavenumber $(\bar{\upsilon})$ force constant (k) and bond length (r) calculated for $SrTi_{1-x}FexO_3$

3.3 Field Emission Scanning Electron Microscope

The surface morphology of the $SrTi_{1-x}Fe_xO_3$ nanoceramics was investigated by FE-SEM, as shown in Fig. 3a, b. It is obvious that all samples consist of the cubic structure with an average grain size (G) in the range of $80–140$ nm. The FE-SEM micrographs of the Fe-doped $SrTiO_3$ shows more aggregated grains within its microstructure. The increase in microstrain (ε) as a function of concentration is caused by the grain aggregates which induce the internal stress within the grains. When a fine-grained ceramic is subjected to the field, the grain is subjected to an internal stress, which depends on the orientation of all the surrounding grains. Average grain sizes of $SrTiO_3$ decreases with an increase in Fe concentration. The FE-SEM micrographs are nearly agreed with results estimated by the W–H relation being used to calculate the average crystallite size.

Fig. 3

S-4800 20.0kV 13.7mm x40.0k SE(M) 22/03/2017 14:31   1.00um
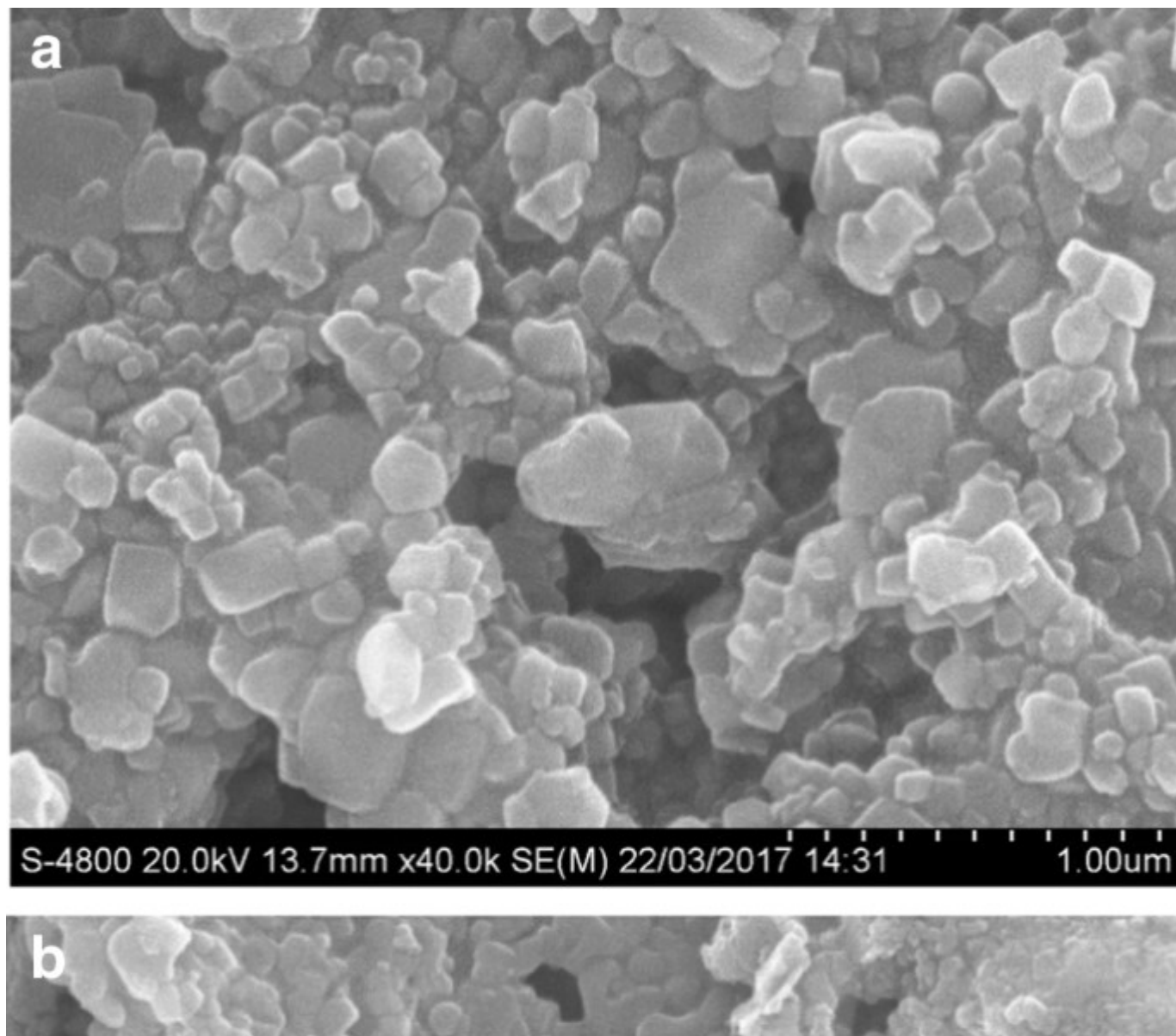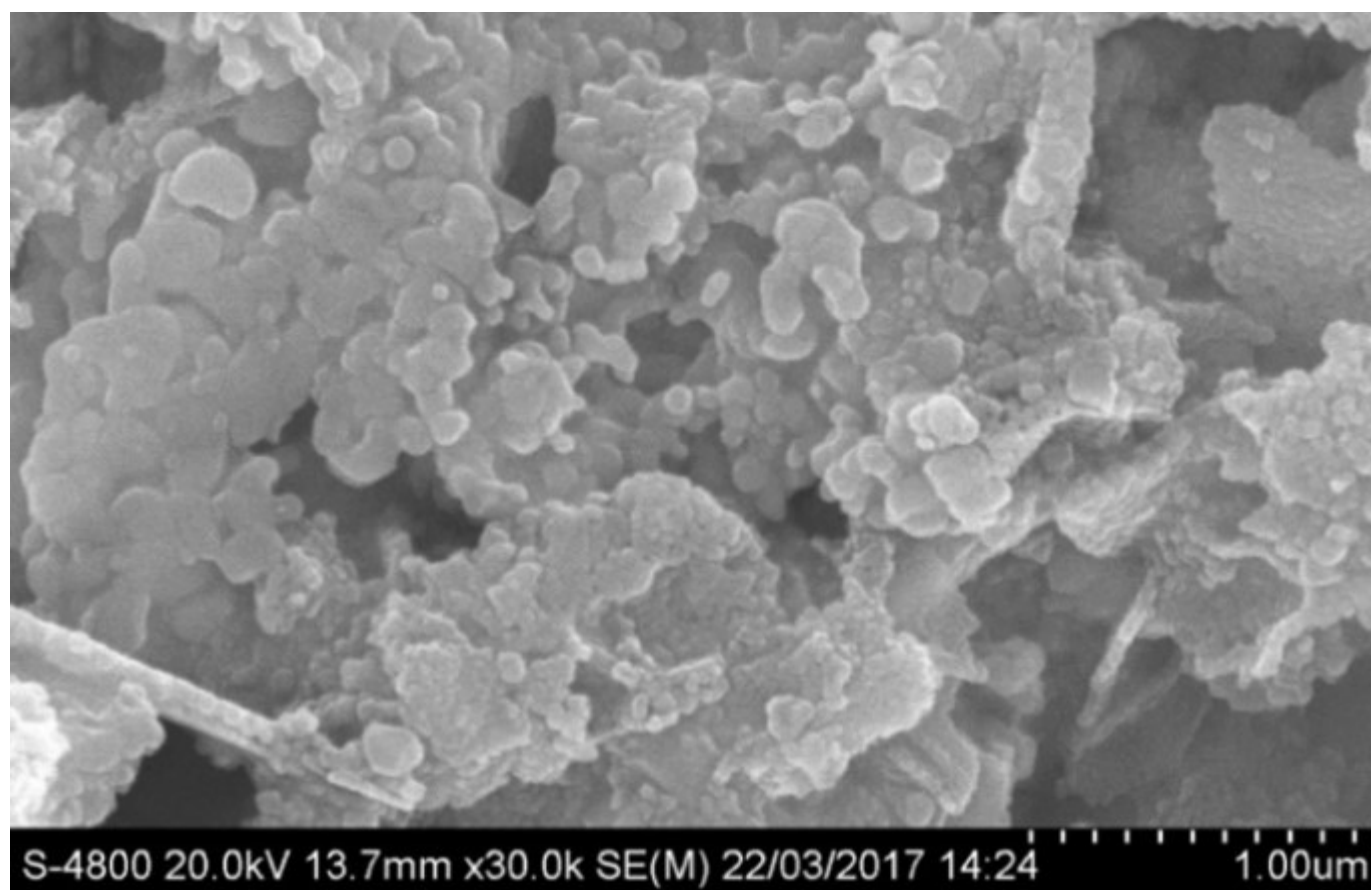
a, b Typical SEM images of $SrTi_{1-x}Fe_xO_3$ (x = 0.0 and 0.1)

Figure 4a, b shows the EDS images of x = 0.0 and 0.1 composition, respectively. As we expected, the concentrations of Fe must be higher for x= 0.1 samples. The EDS analysis shows that Fe concentration increases with a decrease in Ti percentage. The EDS pattern confirmed the presence of Sr^{2+}, Ti^{4+}, and Fe^{3+} element in the expected stoichiometry proportion including a small error. An EDS results also confirmed that precursors that are used for synthesis totally vanish in the chemical reaction $SrTi_{1-x}Fe_xO_3$.

Fig. 4
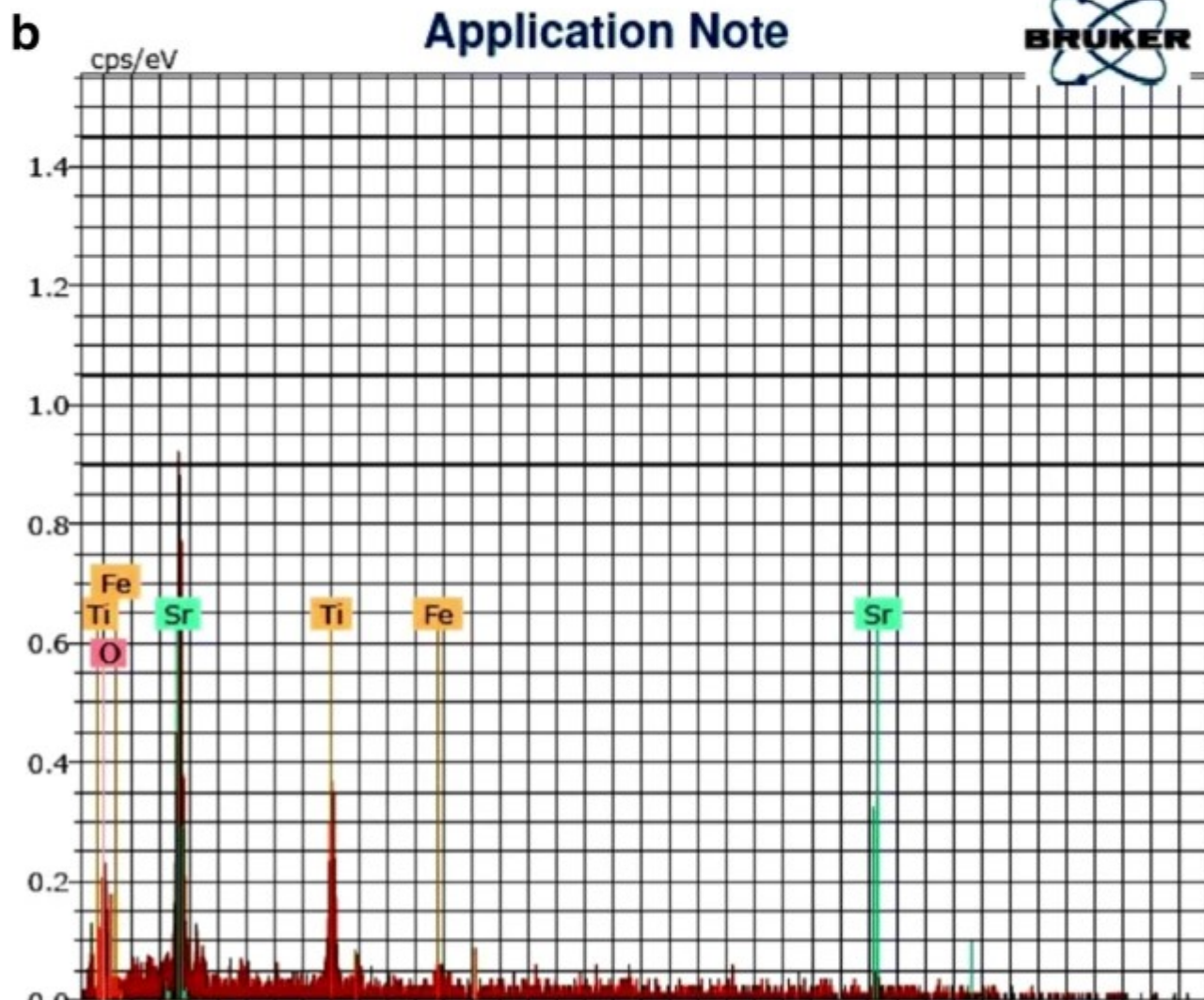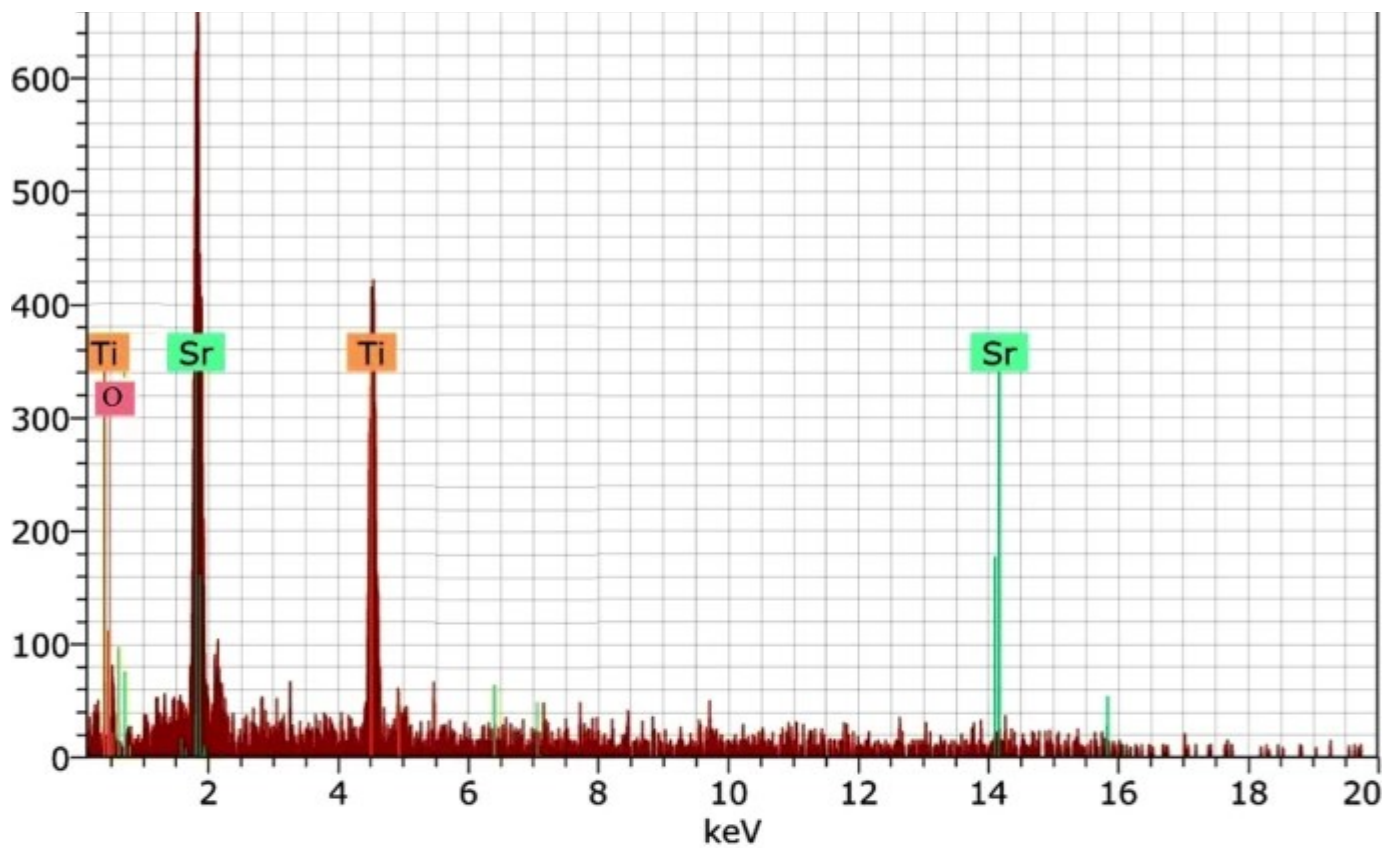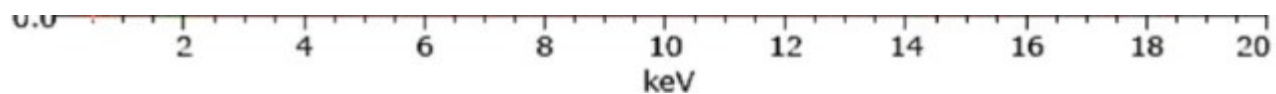
a, b Typical EDS images of $SrTi_{1-x}Fe_xO_3$ (x = 0.0 and 0.1)

3.4 Transmission Electron Microscopy

The transmission electron microscopy (TEM) is a significant technique for the determination of particle size and the particle distribution of the nanoparticles. Figure 5a−d shows a typical TEM micrograph and their corresponding selected area electron diffraction patterns (SAED) of prepared Fe-doped $SrTiO_3$ nanoceramic materials. In TEM images, the nanoparticles are approximately cubic and spherical in shape with very small agglomeration also being observed. It is observed that the average particle size of pure and Fe-doped $SrTiO_3$ is in the range of 34−72 nm, which is in good agreement with the XRD results. The corresponding SAED pattern consists of concentric sharp rings of well-resolved diffraction planes which confirm the cubic structure of $SrTiO_3$. Also, the SAED pattern shows the superimposition of the bright spots with Debye ring pattern indicating the crystalline nature of the present samples.

Fig. 5
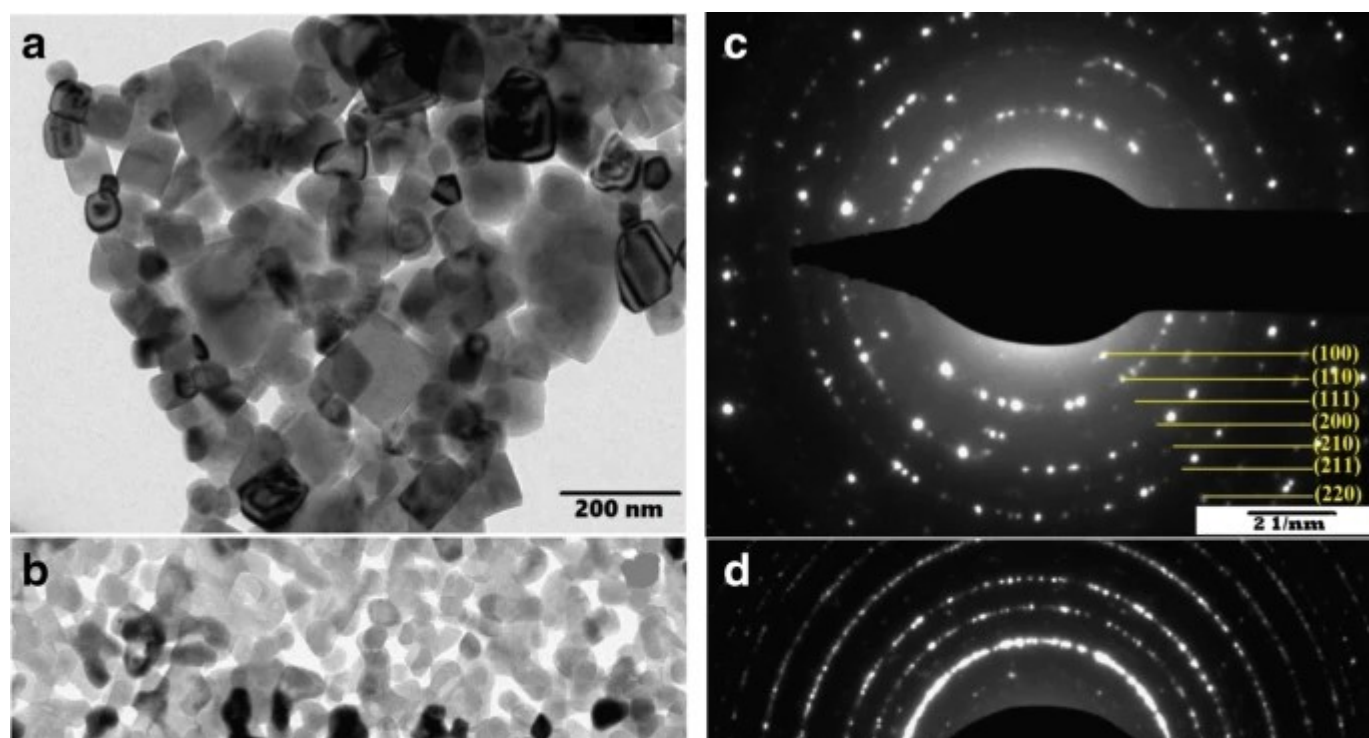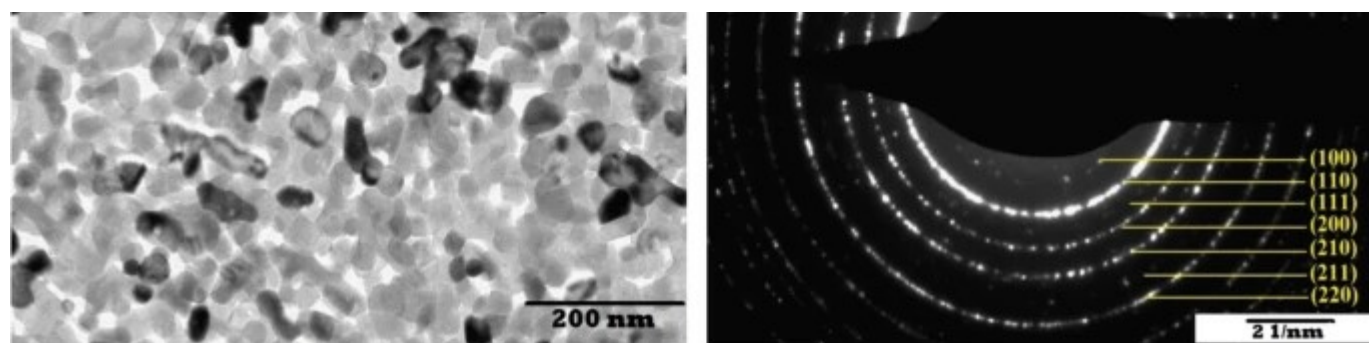
a, b Typical TEM images and c, d respective SEAD pattern of $SrTi_{1-x}Fe_xO_3$ for (x = 0.0 and 0.1)

3.5 Dielectric Study

The dielectric properties can be obtained by measuring the capacitance (C) of the Fe–doped $SrTiO_3$ at room temperature using LCR-Q meter (Hewlett Packard, Model 4284-A) in the frequency range of 50 Hz−1 MHz. The values of the dielectric constant (ε') were calculated by using the following relation [35];

$$ \varepsilon^{\prime}=\frac{\text{Cd}}{\epsilon_{0} A} $$

(13)

where C is the capacitance in farad, d is the thickness of pellet, A is the cross-sectional area of the pellet, and ε_0 is constant permittivity free space (ε_0 = 8.85 × 10^{-12} F m^{-1}). C was measured in the variable frequency at room temperature. A variation of the dielectric constant (ε') as a function of frequency at room temperature is shown in Fig. 6a. It shows that the dielectric constant decreases exponentially with increasing frequency which exhibits a normal dielectric dispersion. Exchange electrons between Fe^{2+} and Fe^{3+} ions lead to the decrease in dielectric constant (ε') with frequency, which remains constant for higher frequency. The high value of the dielectric constant at low frequencies is due to the accumulation of charges at the interfaces between the sample and the electrodes. The observed dielectric behavior of the present sample can be explained on the basis of Koop's model and Maxwell–Wagner polarization [36, 37]. As the frequency increases, the dipoles in the samples reorient themselves instantly to respond to the applied electric field resulting in the increase in ε' at higher frequencies. On the other hand, at higher frequencies, it has been observed that the

dielectric constant value decreases as the Fe content changes from x = 0.1 to 0.4, which is attributed due to the decrease in the grain size.

Fig. 6
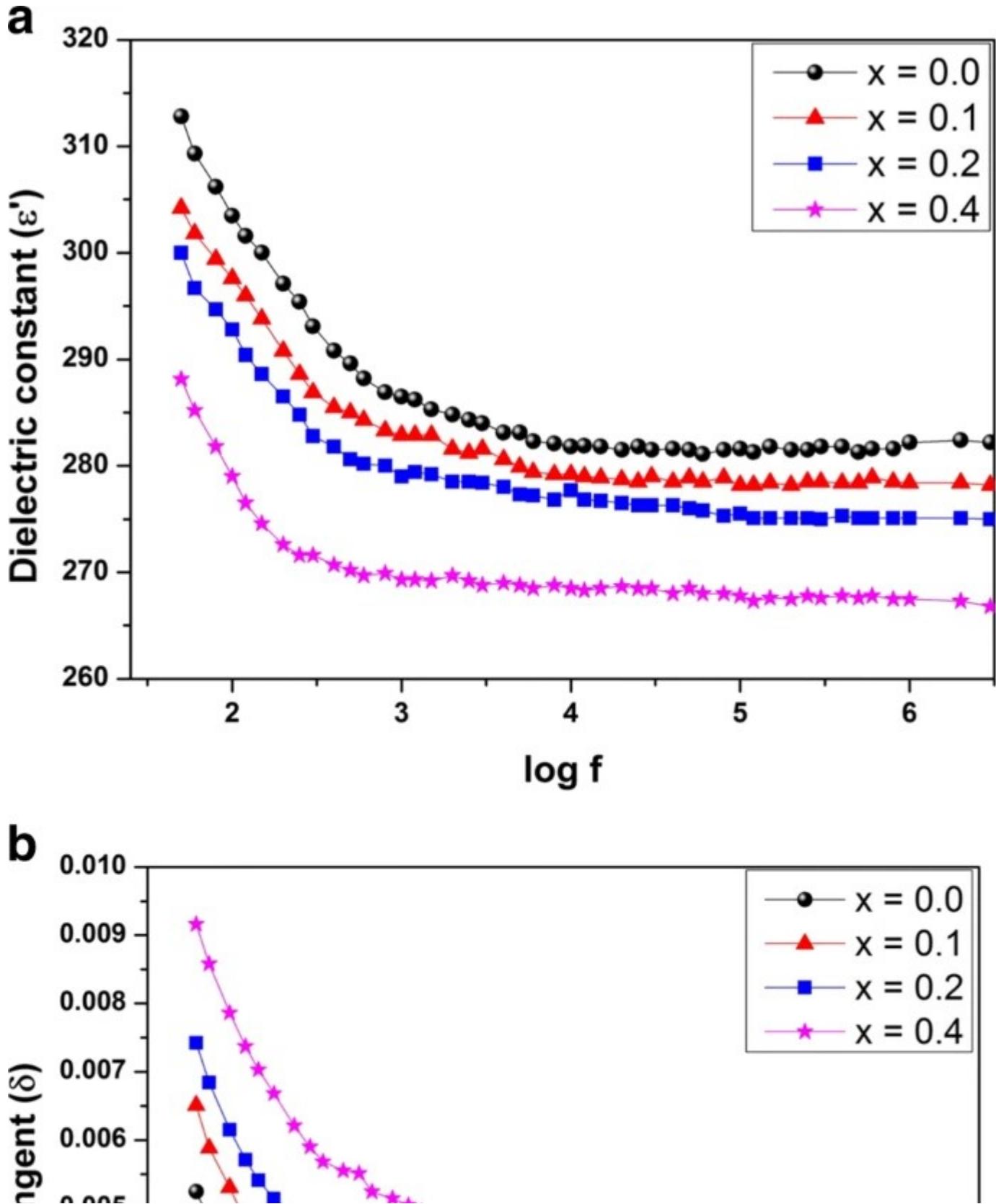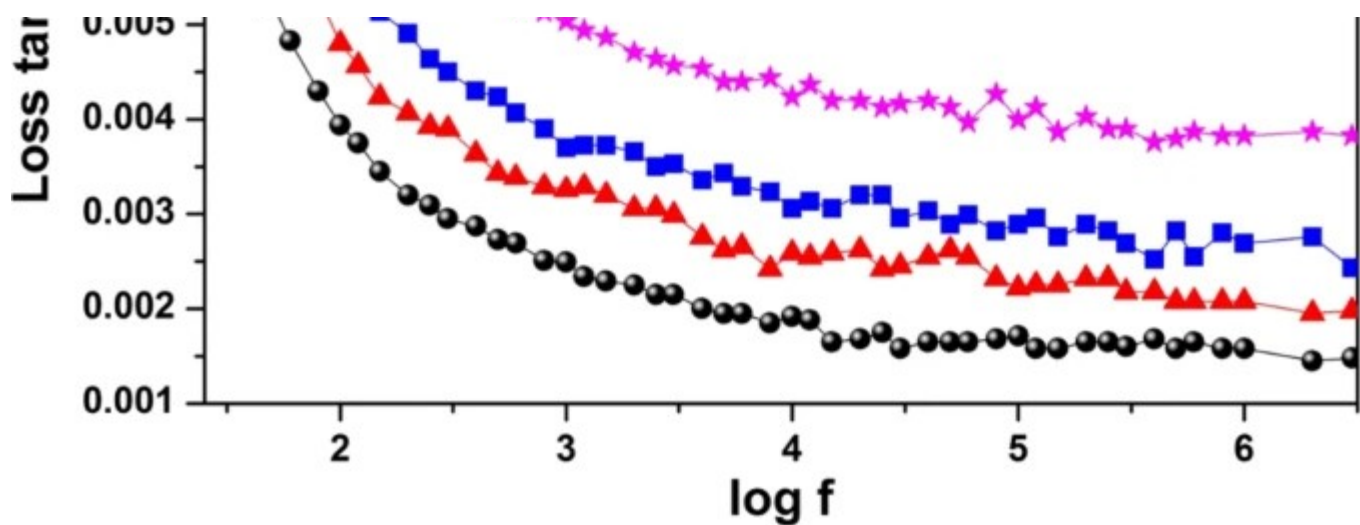
a Variation of dielectric constant ($\varepsilon^{\prime}$) for $SrTi_{1-x}Fe_xO_3$ (x = 0.0, 0.1, 0.2, and 0.4). b Variation of dielectric loss tangent ($\tan\delta$) for $SrTi_{1-x}Fe_xO_3$ (x = 0.0, 0.1, 0.2, and 0.4)

The FE–SEM micrographs of the Fe–doped $SrTiO_3$ shows more aggregated grains within its microstructure. The decrease in dielectric constant as a function of concentration is due to the grain boundary aggregation, which induces the internal stress within the grains. When a fine-grained ceramic is subjected to the field, the grain is subjected to an internal stress, which depends on the orientation of all the surrounding grains. Thus, the decrease in dielectric constant is observed; the stress system would tend to suppress the spontaneous deformation and force the grain back toward the cubic state [38, 39].

For higher frequencies, the dielectric constant remains constant and independent of frequency. Since electric dipoles produced in the material does not increase by the applied electric field. The initial increase in dielectric constant can be attributed to the polarization of space charge accumulation on the surface of dielectric materials. In high-frequency region, the small duration is required to assemble the space charge carriers and its orientation in response to the applied electric field. Hence, if the frequency of the reverse field increases, the dielectric constant decreases [40]. The high values of the dielectric constant of the present $SrTiO_3$ material at a lower frequency may be due to the heterogeneous hopping mechanism to low-frequency dispersion. The dielectric behavior of the $SrTiO_3$ material is also similar to the literature reports [13]. It is also observed that the dielectric constant is decreased with the increase in the doping concentration x. This might be occurring from a decrease in the grain

size by doping concentration of Fe content in $SrTiO_3$. The variation of dielectric loss tangent ($\tan\delta$) as a function of frequency is shown in Fig. 6b. It is observed that dielectric loss tangent ($\tan\delta$) values show the similar behavior as the dielectric constant.

3.6 DC Conductivity

Figure 7 shows the DC conductivity graph of Fe-doped $SrTiO_3$ samples. DC conductivity was measured using the two-probe method against varying temperatures. It shows the increase in electrical conductivity with temperature obeying the Arrhenius relation. The increase in the conductivity of the given sample is in accordance with the ion hopping mechanism which indicates a p-type semiconducting nature. The conductivity of Fe-doped $SrTiO_3$ strongly depended on three factors: pressure, temperature, and Fe-doping concentration. At low pressure, oxygen vacancy of the p-type semiconductor forming an electron–hole pair creates an n-type majority electron charge carrier. As the pressure reaches to 100 Pa, an increase in conductivity is shown due to the p-type majority hole charge carriers. Also, it is found that the increase in mobility of charge carriers is due to the thermal activation of charge carriers. It can also be due to the lattice vibration which helps the ions to come closer to each other. This leads to a strong correlation between mobility and conductivity and supports the increase in the probability for hopping mechanism of the free electrons to fit the adjacent octahedral site. The increase in mobility of charge carriers implies an increase in conductivity and decrease in resistivity.

Fig. 7
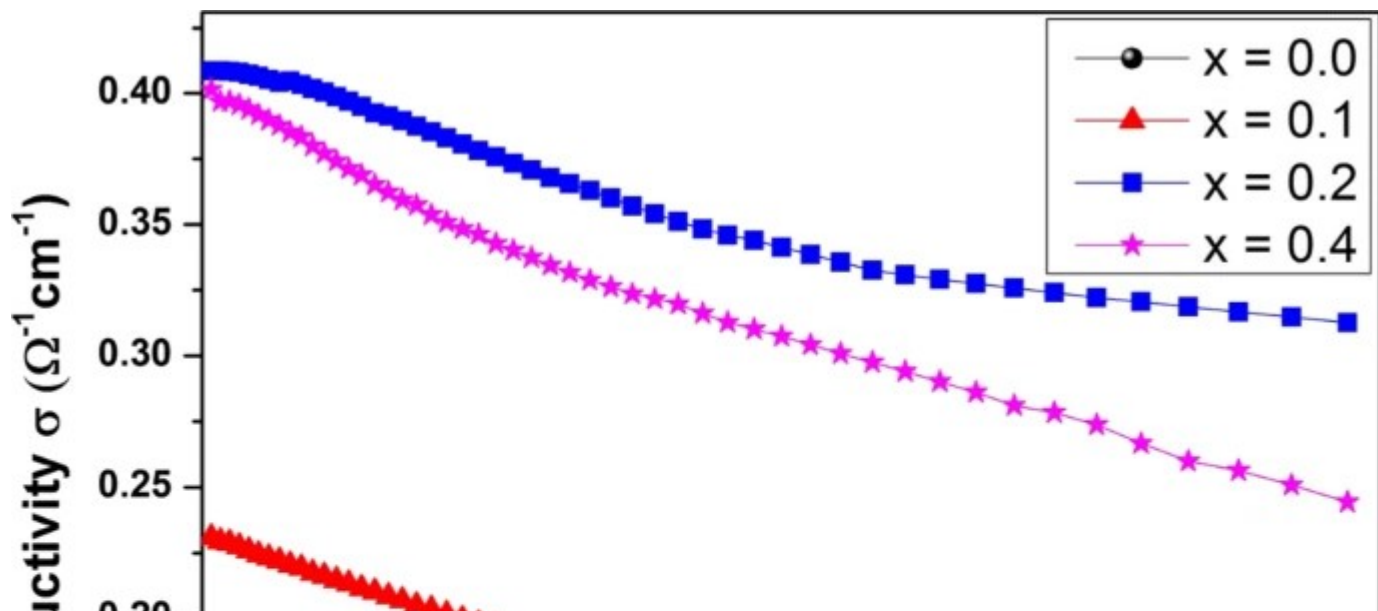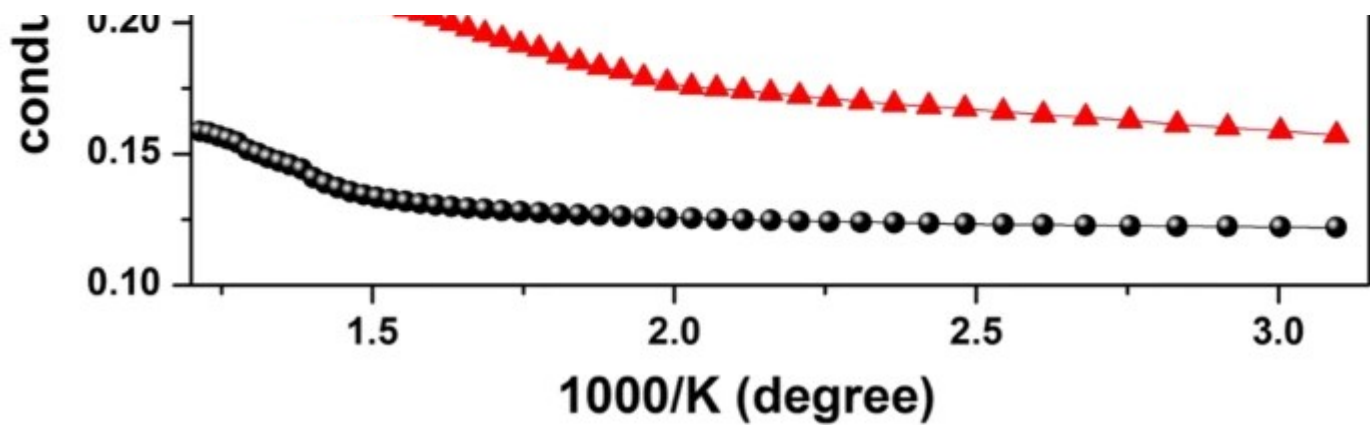
Variation of DC conductivity for $SrTi_{1-x}Fe_xO_3$ (x = 0.0, 0.1, 0.2, 0.3, 0.4, and 0.5)

The variation of mobility with temperature is shown in Fig. 8. Earlier, several reports strongly recommend that the enhancement in the conductivity of the Fe-doped $SrTiO_3$ material was found due to the increase in the large grain boundaries. Also, it may be due to an increase in oxygen and deflection vacancies which leads to an increase in the conductivity on both sides of each grain boundary [41]. Figure 7 shows that conductivity increases from x = 0.0 to 0.2 due to the increases in grain size, but according to Claus et al., at high doping concentration, in accepter-doped $SrTiO_3$ reduces electron hole concentration due to the ionization reaction contributing to the decrease in the conductivity up to certain limits. This result is consistent with observed FE–SEM results [42].

Fig. 8
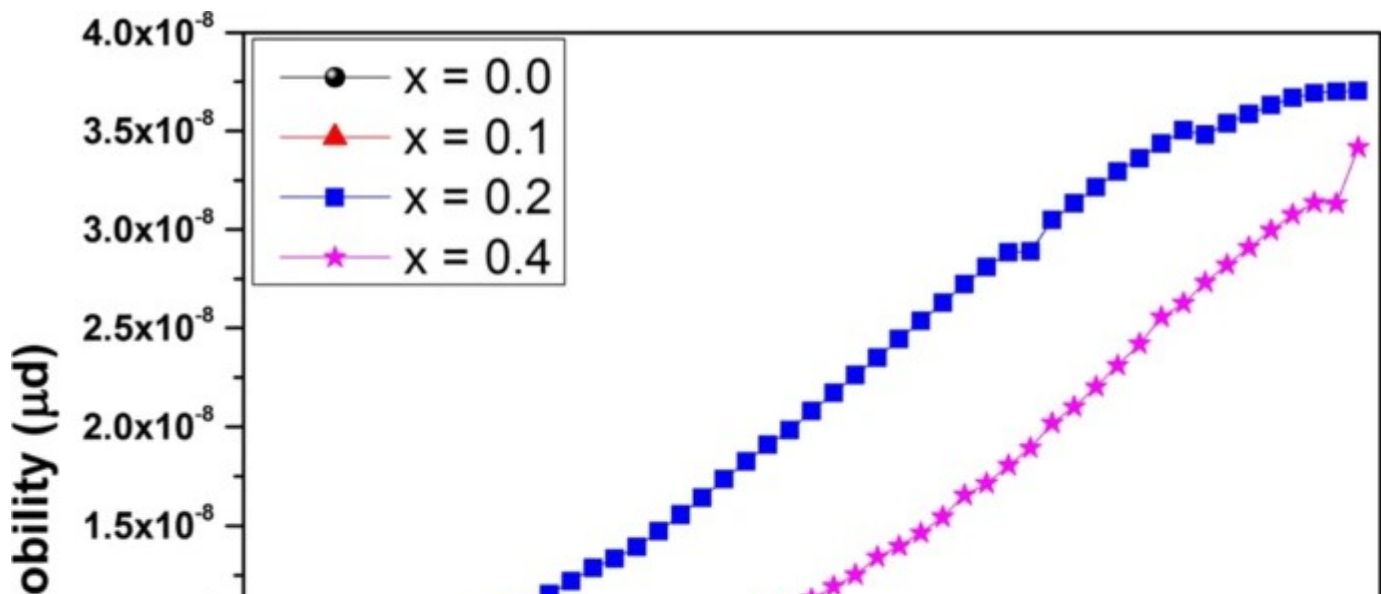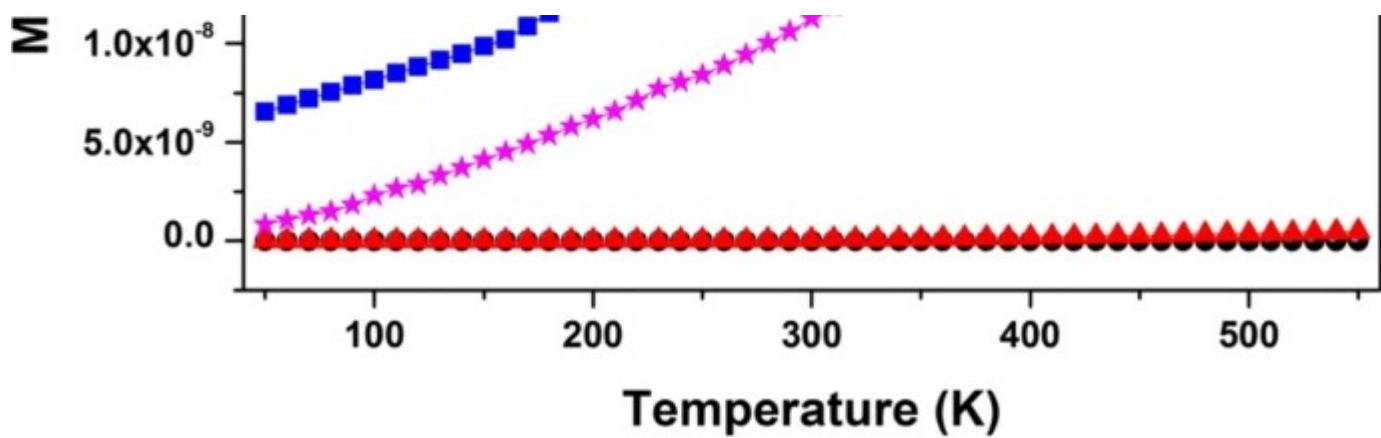
Variation of mobility for $SrTi_{1-x}Fe_xO_3$ (x = 0.0, 0.1, 0.2, and 0.4)

The introduction of Fe ions in $SrTiO_3$ would be replacing the Ti ions and create electron or hole charge carrier vacancies. This vacancy plays an important role in the conduction mechanism and increases the electrical conductivity of Fe–Doped $SrTiO_3$ structure. The increased amount of charge carrier in the material depends on the doping concentration and synthesis condition. An increase in the Fe concentration promotes oxygen vacancies, and it participates as one of conducting species in the specimen. The main reason for the formation of the defect is due to the different valence states of the Ti and Fe ion. The defect produced in the Fe-doped $SrTiO_3$ can be easily understood using Kroger-Vink notations [43].

$$ 2\text{SrO}+{\text{Fe}}_{2}O_{3}= 2{\text{Sr}}_{\text{Sr}}^{x}+ 2{\text{Fe}}_{\text{Ti}}^{\prime}+ 5\mathrm{O}_{o}^{x}+\mathrm{V}_{O}^{\circ \circ} $$
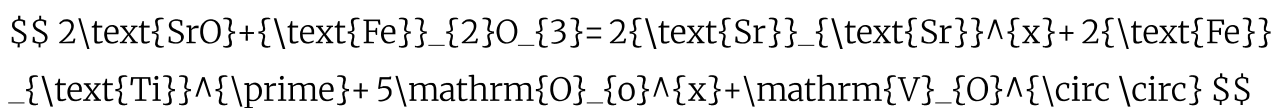
(14)

where $({\text {Fe}}_{\text {Ti}}^{\prime })$ is accepter impurity and $(\mathrm {V}_{O}^{\circ \circ })$ are oxygen vacancies.

The electroneutrality in the above equation;

$$ \frac{1}{2}[{\text{Fe}}_{\text{Ti}}^{\prime}]=[\mathrm{V}_{O}^{\circ \circ}]=\text{constant} $$

(15)

But oxygen vacancy is equilibrium with oxygen gas and electron hole $\dot{(h)}$;

$$ \mathrm{V}_{O}^{\circ \circ}+\frac{1}{2}\mathrm{O}_{2}(g)=\mathrm{O}_{O}^{x}+2\dot{h} $$

(16)

$$ K_{a}=p^{2}{[\mathrm{V}_{O}^{\circ\circ}]}^{-1}p\mathrm{O}_{2}^{-\frac{1}{2}} $$

(17)

From ([15](#)) and ([17](#)), the defect of the electron and electron–hole concentration can be calculated as;

$$ p=\frac{K_{i}}{n}=\frac{1}{\sqrt 2} K_{a}^{\frac{1}{2}}{[{\text{Fe}}_{\text{Ti}}^{\prime}]}^{\frac{1}{2}}p\mathrm{O}_{2}^{\frac{1}{4}} $$

(18)

Since intrinsic ionization of electrons ($n \times p = K_i$) are equilibrium, the electron holes correlate with a lattice species as the dopant Fe;

$$ {\text{Fe}}_{\text{Ti}}^{\prime}+\dot{h}={\text{Fe}}_{\text{Ti}}^{x} $$

(19)

and oxygen lattice.

$$ \mathrm{O}_{O}^{x}+\dot{h}=\dot{O_{O}} $$

(20)

The increase in electric conductivity it may attribute to the decrease in activation and band-gap energy as a doping concentration of Fe in $SrTiO_3$.

3.7 Vibrating Sample Magnetometer

The magnetic property of Fe-doped $SrTiO_3$ samples has been investigated by the VSM technique at room temperature for 20 kOe applied magnetic fields. The field- dependent magnetization of $SrTi_{1-x}Fe_xO_3$ samples is shown in Fig. 9. The magnetic behavior of pure $SrTiO_3$ is paramagnetic in nature, which may be due to the oxygen vacancies inducting magnetism in pure $SrTiO_3$ or large average distance of dopant Fe ions [44, 45]. The graph of pure $SrTiO_3$ is shown in the inset of Fig. 9. But (M−H) loops of the Fe-doped samples have diluted ferromagnetic nature with small remanence magnetization and high coercivity (H_c). The highest values of saturation magnetizations (M_s) were observed at x = 0.4 given in Table 3 for the samples with concentration x = 0.1 and 0.2, respectively. Still, the M−H plot does not saturate even after 20 kOe applied in the magnetic field. M_s were increased with Fe concentration in $SrTiO_3$. Values of H_c increases for x = 0.1 to 0.2 concentrations, which is 150.59 to 170.13 Oe then decreases for x= 0.4 concentration. The remanence magnetization M_r values were low for all the samples.

Fig. 9
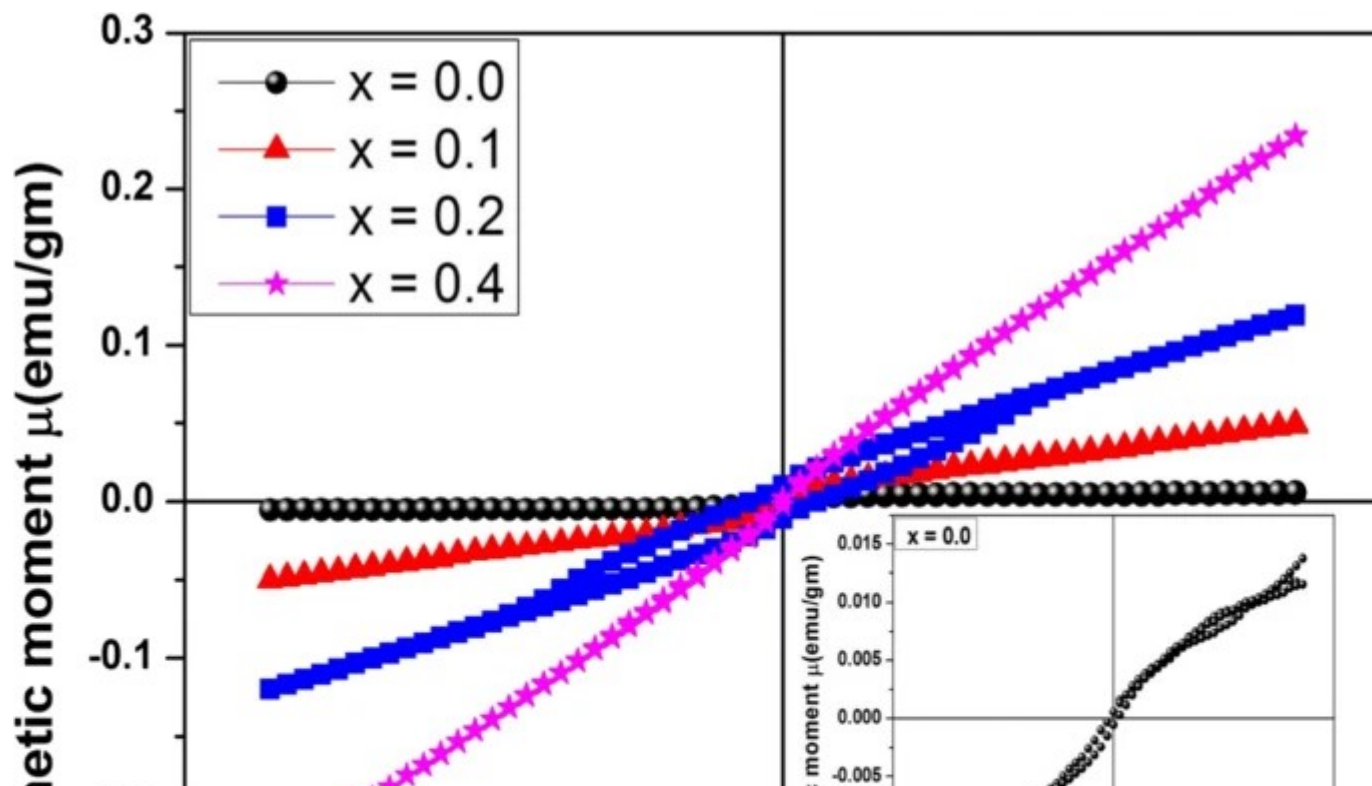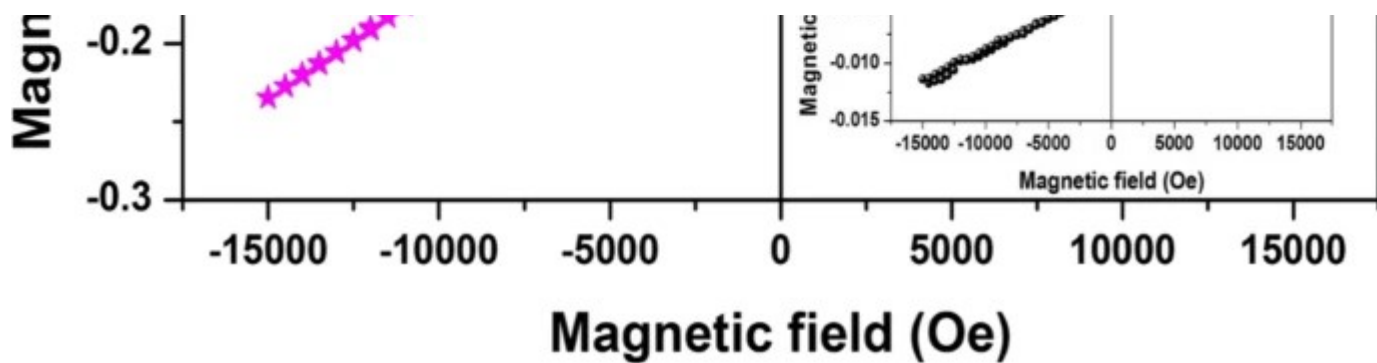
Room temperature magnetic hysteresis loops (M–H) obtained for the $SrTi_{1-x}Fe_xO_3$ (x = 0.0, 0.1, 0.2, and 0.4)

Table 3 Saturation magnetization (M_s), coercivity (H_c), remanence magnetization (M_r), anisotropy constant (K), and anisotropy field (H_K)

The reason of induced ferromagnetism may be due to the double exchange interaction between Fe^{3+}–Fe^{4+}, pentahedral–pentahedral Fe^{3+} interaction, pentahedral-octahedral Fe^{3+} interaction, and octahedral–octahedral Fe^{3+} interaction. The magnetic interactions depend on a number of conduction carriers and the distance between neighboring nuclei [46]. This can be explained on the basis of Ruderman–Kittel–Kasuya-Yosida (RKKY) model.

$$ J_{\text{ij}}^{\text{RKKY}}=J_{0}r^{-4}[\sin(2k_{\mathrm{f}}r)-2k_{\mathrm{f}}r\cos(2\mathrm{k}_{\mathrm{f}}r)] $$

(21)

where $J_{\text{ij}}^{\text{RKKY}}$ is RKKY interactions between two magnetic atoms, r is the distance between the magnetically coupled magnetic atoms, k_f is the Fermi wave vector of carrier density, and J_0 is coupling strength, which is always positive. In this type of magnetism, travelling charge carriers play an important role in magnetization. The anisotropy constant (K) and anisotropy field (H_k) were calculated for each sample using the

following relations [47].

$$ K=\frac{M_{\mathrm{s}}\times H_{\mathrm{c}}}{0.98} $$

(22)

$$ H_{\mathrm{k}}=\frac{{2K}_{1}}{M_{\mathrm{s}}} $$

(23)

An increase in the value of K with an increase in Fe ion concentration in the $SrTiO_3$ matrix is observed, which is responsible for the increased oxygen in vacancies. These oxygen vacancies are acting as a free transporter, and Fe^{3+} ions offer the magnetic moments. Due to oxygen vacancies, super-exchange interaction between neighboring Fe^{3+} ions, i.e., $Fe^{3+}-O^{2-}-Fe^{4+}$ ions occur. As a result, there is an increase in Fe in the magnetic property in the compound. Such type of induced ferromagnetism was also found in other non-magnetic oxides like $BaTiO_3$, ZnO, $BaZrO_3$, etc. [34, 48, 49].

4 Conclusions

Fe-doped $SrTiO_3$ nanoceramic with x = 0.0, 0.1, 0.2, and 0.4 was synthesized using sol-gel autocombustion method. The XRD analysis shows that prepared nanoceramic are having a cubic structure throughout the series without change of phase. The gradual decrease in lattice parameter values is observed due to variation of oxidation state of Fe ions with increase in doping concentration. The metal oxide band found in FT-IR spectra confirms the perovskite structure of the prepared nanoceramic samples. FE-SEM study reveals that the average grain size of samples is in nano-size range with small agglomeration. The dielectric behavior of the samples was affected by oxygen vacancy being produced due to the Fe content. The oxygen vacancy plays an important role in the conduction mechanism and increases the electrical conductivity of Fe content in the $SrTiO_3$ matrix. M-H plot reveals that the magnetization increases with an increase in the Fe content which can be applicable for memory-based application.

References

1. Bahl, C.R., Velazquez, D., Nielsen, K.K., Engelbrecht, K., Andersen, K.B., Bulatova, R., Pryds, N.: High performance magnetocaloric perovskites for magnetic refrigeration. Appl. Phys. Lett. 100, 121905 (2012)

   Article   ADS   Google Scholar

2. Zhang, S., Xia, R., Randall, C.A., Shrout, T.R., Duan, R., Speyer, R.F.: Dielectric and piezoelectric properties of niobium-modified $BiInO_3-PbTiO_3$ perovskite ceramics with high Curie temperatures. J. Mater. Res. 20, 2067–2071 (2005)

   Article   ADS   Google Scholar

3. Shisode, M.V., Bhoyar, D.N., Khirade, P.P., Jadhav, K.: Structural, microstructural, magnetic, and ferroelectric properties of Ba^{2+}-doped $BiFeO_3$ nanocrystalline multifferroic material. J. Supercond. Nov. Magn., 1–9 (2017)

4. Zhao, T., Lu, H., Chen, F., Yang, G., Chen, Z.: Stress-induced enhancement of second-order nonlinear optical susceptibilities of barium titanate films. J. Appl. Phys. 87, 7448–7451 (2000)

   Article   ADS   Google Scholar

5. Niederberger, M., Garnweitner, G., Pinna, N., Antonietti, M.: Nonaqueous and halide-free route to crystalline $BaTiO_3$, $SrTiO_3$, and $(Ba, Sr)TiO_3$ nanoparticles via a mechanism involving C-C bond formation. J. Am. Chem. Soc. 126, 9120–9126 (2004)

   Article   Google Scholar

6. Dietz, G., Schumacher, M., Waser, R., Streiffer, S., Basceri, C., Kingon, A.: Leakage currents in $Ba_{0.7}Sr_{0.3}TiO_3$ thin films for ultrahigh-density dynamic random access memories. J.

Appl. Phys. 82, 2359–2364 (1997)

Article   ADS   Google Scholar

7. Konta, R., Ishii, T., Kato, H., Kudo, A.: Photocatalytic activities of noble metal ion doped SrTiO$_3$ under visible light irradiation. J. Phys. Chem. B 108, 8992–8995 (2004)

Article   Google Scholar

8. Lee, S.W., Kwon, O.S., Han, J.H., Hwang, C.S.: Enhanced electrical properties of SrTiO$_3$ thin films grown by atomic layer deposition at high temperature for dynamic random access memory applications. Appl. Phys. Lett. 92, 222903 (2008)

Article   ADS   Google Scholar

9. Tang, M., Wang, Z., Li, J., Zeng, Z., Xu, X., Wang, G., Zhang, L., Xiao, Y., Yang, S., Jiang, B.: Bipolar and unipolar resistive switching behaviors of sol–gel-derived SrTiO$_3$ thin films with different compliance currents. Semicond. Sci. Technol. 26, 075019 (2011)

Article   ADS   Google Scholar

10. Mochizuki, S., Fujishiro, F., Minami, S.: Photoluminescence and reversible photo-induced spectral change of SrTiO$_3$. J. Phys.: Condens. Matter 17, 923 (2005)

ADS   Google Scholar

11. Zhang, W., Yin, Z., Zhang, M., Du, Z., Chen, W.: Roles of defects and grain sizes in photoluminescence of nanocrystalline SrTiO$_3$. J. Phys.: Condens. Matter 11, 5655 (1999)

ADS   Google Scholar

12. Zhou, X., Shi, J., Li, C.: Effect of metal doping on electronic structure and visible light

absorption of $SrTiO_3$ and $NaTaO_3$ (metal = Mn, Fe, and Co). J. Phys. Chem. C 115, 8305–8311 (2011)

Article **Google Scholar**

13. Haeni, J., Irvin, P., Chang, W., Uecker, R., Reiche, P., Li, Y., Choudhury, S., Tian, W., Hawley, M., Craigo, B.: Room-temperature ferroelectricity in strained $SrTiO_3$. Nature 430, 758 (2004)

Article **ADS** **Google Scholar**

14. Beattie, A., Samara, G.: Pressure dependence of the elastic constants of $SrTiO_3$. J. Appl. Phys. 42, 2376–2381 (1971)

Article **ADS** **Google Scholar**

15. Burn, I., Neirman, S.: Dielectric properties of donor-doped polycrystalline $SrTiO_3$. J. Mater. Sci. 17, 3510–3524 (1982)

Article **ADS** **Google Scholar**

16. Blennow, P., Hagen, A., Hansen, K.K., Wallenberg, L.R., Mogensen, M.: Defect and electrical transport properties of Nb-doped $SrTiO_3$. Solid State Ion. 179, 2047–2058 (2008)

Article **Google Scholar**

17. Neri, G., Bonavita, A., Micali, G., Rizzo, G., Licheri, R., Orru, R., Cao, G.: Resistive λ-sensors based on ball milled Fe-doped $SrTiO_3$ nanopowders obtained by self-propagating high-temperature synthesis (SHS). Sens. Actuators B 126, 258–265 (2007)

Article **Google Scholar**

18. Rothschild, A., Tuller, H.L.: Gas sensors: New materials and processing approaches. J. Electroceram. 17, 1005−1012 (2006)

Article   Google Scholar

19. Waser, R., Baiatu, T., Härdtl, K.H.: dc electrical degradation of perovskite-type titanates. I: Ceramics. J. Am. Ceram. Soc. 73, 1645−1653 (1990)

Article   Google Scholar

20. Liou, Y.-C., Wu, C.-T., Chung, T.-C.: Synthesis and microstructure of $SrTiO_3$ and $BaTiO_3$ ceramics by a reaction-sintering process. J. Mater. Sci. 42, 3580−3587 (2007)

Article   ADS   Google Scholar

21. Allahverdi, M., Hall, A., Brennan, R., Ebrahimi, M., Hagh, N.M., Safari, A.: An overview of rapidly prototyped piezoelectric actuators and grain-oriented ceramics. J. Electroceram. 8, 129−137 (2002)

Article   Google Scholar

22. Galinetto, P., Casiraghi, A., Mozzati, M., Azzoni, C., Norton, D., Boatner, L.A., Trepakov, V.: Magnetic and structural studies in Co-and Mn-implanted $SrTiO_3$ single crystals. Ferroelectrics 368, 120−130 (2008)

Article   Google Scholar

23. Xie, T.-H., Sun, X., Lin, J.: Enhanced photocatalytic degradation of RhB driven by visible light-induced MMCT of Ti (IV)-O-Fe (II) formed in Fe-doped $SrTiO_3$. J. Phys. Chem. C 112, 9753−9759 (2008)

Article   Google Scholar

24. Fukumi, K., Chayahara, A., Kadono, K., Sakaguchi, T., Horino, Y., Miya, M., Hayakawa, J., Satou, M.: Au +-ion-implanted silica glass with non-linear optical property. Jpn. J. Appl. Phys. 30, L742 (1991)

Article   ADS   Google Scholar

25. Miranda, F.A., Subramanyam, G., Van Keuls, F.W., Romanofsky, R.R., Warner, J.D., Mueller, C.H.: Design and development of ferroelectric tunable microwave components for Kuand K-band satellite communication systems. IEEE Trans. Microwave Theory Tech. 48, 1181–1189 (2000)

Article   ADS   Google Scholar

26. Yu, H., Wang, J., Yan, S., Yu, T., Zou, Z.: Elements doping to expand the light response of $SrTiO_3$. J. Photochem. Photobiol. A Chem. 275, 65–71 (2014)

Article   Google Scholar

27. Vinayak, V., Khirade, P.P., Birajdar, S.D., Alange, R., Jadhav, K.: Electrical and dielectric properties of low-temperature-synthesized nanocrystalline Mg^{2+}-substituted cobalt spinel ferrite. J. Supercond. Nov. Magn. 28, 3351–3356 (2015)

Article   Google Scholar

28. Fuentes, S., Muñoz, P., Barraza, N., Chávez-Ángel, E., Torres, C.S.: Structural characterisation of slightly Fe-doped $SrTiO_3$ grown via a sol–gel hydrothermal synthesis. J. Sol-Gel Sci. Technol. 75, 593–601 (2015)

Article   Google Scholar

29. Khirade, P.P., Birajdar, S.D., Humbe, A.V., Jadhav, K.: Structural, electrical and dielectric property investigations of Fe-doped $BaZrO_3$ nanoceramics. J. Electron. Mater. 45, 3227–

3235 (2016)

Article ADS Google Scholar

30. Alange, R., Khirade, P.P., Birajdar, S.D., Humbe, A.V., Jadhav, K.: Structural, magnetic and dielectrical properties of Al−Cr Co-substituted M-type barium hexaferrite nanoparticles. J. Mol. Struct. 1106, 460−467 (2016)

Article ADS Google Scholar

31. Humbe, A.V., Nawle, A.C., Shinde, A., Jadhav, K.: Impact of Jahn Teller ion on magnetic and semiconducting behaviour of Ni-Zn spinel ferrite synthesized by nitrate-citrate route. J. Alloys Compd. 691, 343−354 (2017)

Article Google Scholar

32. Švarcová, S., Wiik, K., Tolchard, J., Bouwmeester, H.J., Grande, T.: Structural instability of cubic perovskite $Ba_xSr_{1-x}Co_{1-y}FeyO_{3-\delta}$. Solid State Ion. 178, 1787−1791 (2008)

Article Google Scholar

33. Jayabal, P., Sasirekha, V., Mayandi, J., Jeganathan, K., Ramakrishnan, V.: A facile hydrothermal synthesis of $SrTiO_3$ for dye sensitized solar cell application. J. Alloys Compd. 586, 456−461 (2014)

Article Google Scholar

34. Khirade, P.P., Birajdar, S.D., Shinde, A., Jadhav, K.: Room temperature ferromagnetism and photoluminescence of multifunctional Fe doped $BaZrO_3$ nanoceramics. J. Alloys Compd. 691, 287−298 (2017)

Article Google Scholar

35. Raghavender, A., Jadhav, K.: Dielectric properties of Al-substituted Co ferrite nanoparticles. Bull. Mater. Sci. 32, 575–578 (2009)

Article Google Scholar

36. El Ata, A.A., Attia, S., Meaz, T.: AC conductivity and dielectric behavior of $CoAl_xFe_{2-x}O_4$. Solid State Sci. 6, 61–69 (2004)

Article ADS Google Scholar

37. George, M., Nair, S.S., Malini, K., Joy, P., Anantharaman, M.: Finite size effects on the electrical properties of sol–gel synthesized $CoFe_2O_4$ powders: deviation from Maxwell–Wagner theory and evidence of surface polarization effects. J. Phys. D Appl. Phys. 40, 1593 (2007)

Article ADS Google Scholar

38. Frey, M., Xu, Z., Han, P., Payne, D.: The role of interfaces on an apparent grain size effect on the dielectric properties for ferroelectric barium titanate ceramics. Ferroelectrics 206, 337–353 (1998)

Article Google Scholar

39. Sagar, R., Madolappa, S., Sharanappa, N., Raibagkar, R.: Synthesis, structure and electrical studies of praseodymium doped barium zirconium titanate. Mater. Chem. Phys. 140, 119–125 (2013)

Article Google Scholar

40. Ramirez, A., Subramanian, M., Gardel, M., Blumberg, G., Li, D., Vogt, T., Shapiro, S.: Giant dielectric constant response in a copper-titanate. Solid State Commun. 115, 217–220 (2000)

Article　ADS　Google Scholar

41. Yu, Z., Shi, P., Wu, X., Ren, W.: Structural and electrical properties of $SrFe_x Ti_{1-x}O_3$ (x = 0.001, 0.005 and 0.01) thin films prepared by pulsed laser depositions. Ceram. Int. 41, S223–S227 (2015)

Article　Google Scholar

42. Verma, A., Thakur, O., Prakash, C., Goel, T., Mendiratta, R.: Temperature dependence of electrical properties of nickel–zinc ferrites processed by the citrate precursor technique. Mater. Sci. Eng. B 116, 1–6 (2005)

Article　Google Scholar

43. Tai, L. -W., Nasrallah, M., Anderson, H., Sparlin, D., Sehlin, S.: Structure and electrical properties of $La_{1-x}Sr_xCo_{1-y}Fe_yO_3$. Part 1. The system $La_{0.8}Sr_{0.2}Co_{1-y}Fe_yO_3$. Solid State Ion. 76, 259–271 (1995)

Article　Google Scholar

44. Zhang, Y., Hu, J., Cao, E., Sun, L., Qin, H.: Vacancy induced magnetism in $SrTiO_3$. J. Magn. Magn. Mater. 324, 1770–1775 (2012)

Article　ADS　Google Scholar

45. Karaphun, A., Hunpratub, S., Swatsitang, E.: Effect of annealing on magnetic properties of Fe-doped $SrTiO_3$ nanopowders prepared by hydrothermal method. Microelectron. Eng. 126, 42–48 (2014)

Article　Google Scholar

46. Kavokin, K.V.: Anisotropic exchange interaction of localized conduction-band electrons

in semiconductors. Phys. Rev. B 64, 075305 (2001)

Article   ADS   Google Scholar

47. Deshmukh, S., Humbe, A.V., Kumar, A., Dorik, R., Jadhav, K.: Urea assisted synthesis of $Ni_{1-x}Zn_xFe_2O_4$ (0 = x = 0.8): magnetic and Mössbauer investigations. J. Alloys Compd. 704, 227–236 (2017)

Article   Google Scholar

48. Birajdar, S.D., Khirade, P.P., Humbe, A.V., Jadhav, K.: Presence of intrinsic defects and transition from diamagnetic to ferromagnetic state in Co^{2+} ions doped ZnO nanoparticles. J. Mater. Sci. Mater. Electron. 27, 5575–5583 (2016)

Article   Google Scholar

49. Khirade, P.P., Birajdar, S.D., Raut, A., Jadhav, K.: Multiferroic iron doped $BaTiO_3$ nanoceramics synthesized by sol–gel auto combustion: influence of iron on physical properties. Ceram. Int. 42, 12441–12451 (2016)

Article   Google Scholar

Acknowledgments

Author information

Authors and Affiliations

Department of Physics, Dr. Babasaheb Ambedkar Marathwada University, Aurangabad, MS, India

Dhananjay N. Bhoyar, Jitendra S. Kounsalye, Pankaj P. Khirade & K. M. Jadhav

Yeshwantrao Chavan College of Arts, Commerce and Science, Sillod, District, Aurangabad, MS, India

A. A. Pandit

Corresponding author

Correspondence to K. M. Jadhav.

Rights and permissions

Reprints and permissions

About this article

Cite this article

Share this article

Anyone you share the following link with will be able to read this content:

Get shareable link

Provided by the Springer Nature SharedIt content-sharing initiative

Keywords

Nanoceramics   Sol–gel $SrTiO_3$ Williamson–Hall (W–H)   Dielectric

VSM